

## Evidence for a phase transition in an AlCrFe<sub>2</sub>Ni<sub>2</sub> high entropy alloy processed by high-pressure torsion

Xiaotao Liu<sup>1,2\*</sup>, Hua Ding<sup>2\*</sup>, Yi Huang<sup>3,4\*</sup>, Xiao Bai<sup>1,2</sup>, Qian Zhang<sup>1,2</sup>, Haitao Zhang<sup>1,2</sup>, Terence G. Langdon<sup>4</sup>, Jianzhong Cui<sup>1,2</sup>

1. The Key Laboratory of Electromagnetic Processing of Materials, Ministry of Education, Northeastern University, Shenyang, 110819, China

2. State Key Lab of Rolling and Automation, Northeastern University, Shenyang, 110004, China

3. Department of Design and Engineering, Faculty of Science and Technology, Bournemouth University, Poole, Dorset BH12 5BB, UK

4. Materials Research Group, Department of Mechanical Engineering, University of Southampton, Southampton SO17 1BJ, UK

### Abstract:

An as-cast AlCrFe<sub>2</sub>Ni<sub>2</sub> high entropy alloy consisting of face-centered cubic (FCC), ordered body-centered cubic (B2) and body-centered cubic (BCC) solid solution phases was processed by high-pressure torsion (HPT) for up to 1 turn at room temperature and inspection after processing revealed a transition from the B2 and/or BCC phase to the FCC phase. An analysis by energy dispersive spectrometry showed that a reasonably homogeneous chemical composition was obtained when applying a sufficient level of torsional strain which supports the diffusional nature of the transformation. Processing by HPT gave an increase in hardness and strength but a decrease in the measured elongation in tensile testing at room temperature. The enhanced hardness and strength are due to a combination of factors including work hardening, solid solution strengthening and grain boundary strengthening. By analogy with the mechanical alloying process, it is proposed that the phase transition driven by HPT is a direct consequence of the severe shear strain which induces diffusional alloying.

**Key words:** Hardness; High entropy alloys; High-pressure torsion; Phase transition; Strength

**Corresponding author:** Xiaotao Liu ([liuxt@mail.neu.edu.cn](mailto:liuxt@mail.neu.edu.cn)),  
Hua Ding ([dingh@smm.neu.edu.cn](mailto:dingh@smm.neu.edu.cn)),  
Yi Huang ([yhuang2@bournemouth.ac.uk](mailto:yhuang2@bournemouth.ac.uk))

## 1. Introduction

Despite their remarkably concentrated chemistry, high-entropy alloys (HEAs) represent a novel class of compositionally complex metallic materials with simple solid solution structures of FCC, BCC and HCP phases [1-3]. Since their discovery over a decade ago, HEAs have attracted a high level of interest in the scientific community due to their remarkable properties and potential engineering applications [4-7]. The early efforts in this field were mainly aimed at designing HEAs with a crystalline entropy-stabilized single-phase solid solution structure with four or more principal components in an equi-atomic or near equi-atomic ratio [8, 9]. However, HEAs with a single FCC solid solution phase usually have good ductility but low strength whereas those with a single BCC solid solution phase generally exhibit high strength but poor ductility [10, 11]. From an engineering perspective, HEAs with a single phase solid solution structure may not provide the well-balanced mechanical strength and the ductilities required for structural materials. Therefore, inspired by the development of traditional metals and alloys, multi-phase HEAs with tailored properties have been proposed to overcome the trade-off between strength and ductility. Specifically, non-equi-atomic lamellar eutectic high-entropy alloys (EHEAs) consisting of both ductile FCC phases and hard BCC phases were developed and this gives a good combination of high strength and high ductility in the as-cast state [12-17]. It is now envisaged that thermo-mechanical processing may be an effective strategy for further enhancing the overall mechanical properties of these EHEAs [18].

Among the various processing procedures using severe plastic deformation (SPD), high-pressure torsion (HPT) is considered the most effective method for introducing significant grain refinement in a wide range of initially coarse-grained metallic materials. During HPT

processing, a disk-shaped sample is constrained between two massive anvils under high pressure and subjected to concurrent torsional straining [19]. The deformation of materials in such a confined space produces very high strain values without breaking the samples and, after a certain strain value is reached, there is a reasonable dynamic equilibrium between the deformation-driven generation of crystal defects and their recovery. As a result, various phase transformations may be obtained such as the formation or decomposition of a supersaturated solid solution, the dissolution of phases, the disordering of ordered phases, the amorphization of crystallization phases, the synthesis of low temperature, high temperature or high-pressure allotropic modifications and nanocrystallization in the amorphous matrix. These occur in addition to significant grain refinement, particularly in dual or multi-phase materials [20-33].

For HPT processing of traditional alloys, the effect of HPT on microstructural refinement and the properties of single-phase HEAs has been investigated extensively [34-43]. However, compared to other traditional metallic materials, investigations of the microstructural response of HEAs to HPT processing remain fairly limited and there appear to be no reports monitoring the phase transitions and their correlations with the mechanical properties during the HPT processing of EHEAs. A fundamental exploration of the HPT-induced microstructural and phase evolutions of such multi-phase HEAs is important both scientifically and technologically. Accordingly, the present research was initiated to evaluate the impact of HPT deformation on the overall microstructural evolution, phase transitions and the correlations with mechanical properties of an AlCrFe<sub>2</sub>Ni<sub>2</sub> high-entropy alloy.

## **2. Experimental material and procedures**

Alloy ingots with nominal compositions of AlCrFe<sub>2</sub>Ni<sub>2</sub> (at.%) were prepared by arc-

melting a mixture of pure metals having purities above 99.9 wt% in a Ti-gettered high-purity argon atmosphere on a water-cooled Cu hearth. The ingots were remelted at least five times to improve the chemical homogeneity. Polished disks, 10 mm in diameter and 0.82 mm in thickness, were cut by electro-discharge machining (EDM) from the alloy ingot and the disks were processed by HPT for 1/4, 1/2 and 1 turn at room temperature under an applied pressure of 6.0 GPa at 1 rpm using quasi-constrained conditions in which there is a small outflow of material around the periphery of the disk during straining [44]. The equivalent von Mises strain,  $\varepsilon_{eq}$ , developed during HPT was calculated using the equation.

$$\varepsilon_{eq} = \frac{2\pi rN}{\sqrt{3}h} \quad (1)$$

where  $r$  is the distance from the center of the disk,  $N$  is the number of turns and  $h$  is the sample thickness.

The solidification calculation of the experimental alloy was performed using JmatPro 5.0 with a NiFe-base superalloy database. The microstructure was examined in the initial as-cast state and at the center and near the periphery of the HPT-processed disks where the imposed strain values were the lowest and the highest, respectively. The microstructure and the spatial distribution of chemical compositions of the as-cast alloy and HPT-processed alloys were evaluated using scanning electron microscopy (SEM) with energy dispersive spectrometry (EDS). Before SEM/EDS analysis, the surfaces of the samples were mechanically polished to a mirror-like quality with 1200 grit SiC abrasive papers and then the polishing was continued with a colloidal silica suspension with a particle size of 40 nm. The evolution of phase assemblages and phase transitions were determined over the whole surfaces of the disks by using X-ray diffraction (XRD) employing Cu  $K\alpha$  radiation at 45 kV and a tube current of 200

mA with Rigaku SmartLab equipment. The XRD measurements were performed over an angular range  $2\theta$  from  $20^\circ$  to  $100^\circ$  using a scanning step of  $0.01^\circ$  and a scanning speed of  $2^\circ \text{ min}^{-1}$ . The lattice constants of the samples were derived by analysing the XRD line profiles using the Jade 5.0 software.

Microhardness measurements were taken using a Vickers microhardness tester with a load of 500 gf and dwell time of 10 s. The microhardness values, Hv, were measured along randomly selected diameters at intervals of 0.5 mm on each disk. The tensile properties were examined at room temperature on the as-cast alloy and those after HPT processing. Miniature dog-bone-shaped tensile samples with gauge dimensions of  $2.0 \times 1.0 \times 0.8 \text{ mm}^3$  were cut by EDM from symmetric off-center positions (2 mm from the disk center) in each disk. Tensile samples with the same dimensions were also prepared from the as-cast alloy to provide a reliable comparison. Uniaxial tensile tests were performed at room temperature using a dedicated tensile stage for the miniature samples at a strain rate of  $5 \times 10^{-4} \text{ s}^{-1}$  with an AG-X100kN universal testing machine. The yield strength (YS) and ultimate tensile strength (UTS) were derived directly from the corresponding engineering stress-strain curves recorded for each sample. The elongations to failure of each sample were determined by carefully measuring the gauge lengths before and after tensile testing using an optical microscope.

### **3. Experimental results**

#### *3.1 Microstructure and phase assemblage of the as-cast alloy*

Prior to the microstructural examinations, solidification calculations of the AlCrFe<sub>2</sub>Ni<sub>2</sub> alloy were conducted and the results are shown in Fig. 1(a). It can be seen that the solidification

of the alloy starts with a pre-eutectic phase having an FCC structure at the liquidus temperature of 1346°C, followed by the formation of a binary FCC+B2 eutectic at a temperature of 1318°C and lastly the formation of a ternary FCC+B2+BCC eutectic at a temperature of 1311°C which is only 1°C above the solidus temperature of 1310°C where the solidification is completed.

Fig. 1(b) and (c) show back-scattered electron (BSE) images of the microstructure of the as-cast AlCrFe<sub>2</sub>Ni<sub>2</sub> alloy. There are three typical morphologies marked as A, B and C, respectively, in Fig. 1(b). Using SEM-EDS elemental mapping, a partial area of Fig. 1(b) is given in Fig. 2 which shows clearly the inhomogeneous chemical elemental distribution in the initial as-cast alloy. The chemical composition measured for region A and the B2 halo are listed in Fig. 1(b). In region A there are coarse phases which delineate the grain boundaries that are rich in Cr and Fe while the halo surrounding regions A, as indicated by the arrow in Fig. 1(b), is rich in Al and Ni. Generally, the presence of more Fe and Cr give priority to form FCC phases while more Al and Ni leads preferentially to the formation of ordered BCC (B2) phases [45]. Region B in Fig. 1(b) consists of a fine lamellar microstructure corresponding to binary FCC+B2 eutectics. The enlargement of region C in Fig. 1(c) shows ultrafine network-like phases corresponding to the ternary FCC+B2+BCC eutectics. Thus, the phases with light contrast in region C have a FCC structure and those with dark contrast have B2 and BCC structures which cannot be differentiated based on the SEM/EDS level.

The X-ray diffraction (XRD) pattern shown as the bottom curve in Fig. 3(a) demonstrates that the as-cast alloy contains a mixture of FCC, B2 and BCC solid solution phases which is consistent with the solidification calculation and microstructural observations. The minor (100) superlattice diffraction peak represents the formation of the ordered BCC (B2) phase. The

overlapping peaks of the ordered and disordered BCC phases indicate that the lattice parameters of the two phases are close to each other. Based on XRD, SEM/EDS analysis and the solidification calculations, the solidification of the alloy follows the sequence of pre-eutectic FCC phase, FCC+B2 binary eutectics and FCC+B2+BCC ternary eutectics.

It is noted also from the solidification calculations in Fig. 1(a) that a temperature of 1318°C was identified as the last point for the coarsening of the pre-eutectic FCC phases and the onset of nucleation of the binary FCC+B2 eutectics. The temperature of 1311°C was identified as the last point for the coarsening of the binary FCC+B2 eutectics and the beginning of nucleation of the ternary FCC+B2+BCC eutectics. The temperature windows representing the growth time of various phases are 28°C, 7°C and 1°C for the pre-eutectic FCC phases, binary eutectic FCC+B2 phases and ternary eutectic FCC+B2+BCC phases, respectively, and this accounts for the fine eutectic structures especially in the ternary eutectic regions as in Fig. 1(b) and (c). Concerning the formation of the phases in region C, it was attributed to spinodal decomposition in an earlier investigation due to the superposition of the diffraction peaks in the XRD patterns which is a common feature of multi-component systems [46].

### *3.2 Microstructure and phase assemblages of the alloys after HPT processing*

Fig. 3(a) shows the XRD analysis of the AlCrFe<sub>2</sub>Ni<sub>2</sub> alloy in the as-cast condition and after HPT processing through 1/4, 1/2 and 1 turn, respectively. It should be noted that the XRD analyses were performed over the total surfaces of the disks after polishing so that the peaks intensities for the phases represent the averaged values from different areas where the shear straining level along the radius during HPT processing will be different. The XRD patterns of the alloys after HPT processing confirm the presence of FCC, B2 and BCC phases within the

XRD detection limits. However, HPT processing leads to changes in the diffraction intensities and these changes increase with increasing numbers of turns indicating variations in the phase volume fractions. After HPT processing, the intensity of the peaks of the FCC phase increased while that of the B2 and/or BCC phases decreased, suggesting that the volume fraction of the FCC phase increased at the expense of the B2 and/or BCC phases with increasing numbers of turns and therefore with increasing shear strains.

Fig. 3(b) presents enlarged images of the main peaks of the FCC and B2/BCC phases in Fig. 3(a). The occurrence of significant peak broadening of the alloy after HPT processing by reference to the as-cast alloy denotes the introduction of defects, grain fragmentation and internal strain during the HPT processing. Also, the peaks of both the FCC and B2/BCC phases shift rightward continuously with increasing HPT turns and this is consistent with a decrease in the lattice parameters of the separate phases. The calculated lattice constants of the FCC and B2/BCC phases in the as-cast alloy and in the HPT-processed alloys are shown in Fig. 3(c) so that the lattice constants of both the FCC phase and the B2/BCC phase decrease after HPT processing.

Detailed microstructural observations were performed on the HPT-processed disks and the microstructural evolution is documented in Fig. 4 as a function of both the numbers of turns in the vertical columns and the regions of examination in the horizontal rows. Thus, the morphology evolution after HPT processing depends strongly on the position on the disk such that changes at the edge are significantly greater than those at the disk center. The microstructural differences between the centers and the edges of the disks decrease with increasing numbers of HPT turns.

Inspection shows that at the centers of the disks the microstructures of the alloys after HPT processing show the retention of the as-cast morphology after various numbers of turns and appear to be diffuse by comparison with the initial as-cast alloy. For an ideal rigid-body in torsion, the center of the disk is not subjected to any shear strain and therefore the morphology of the phase domains in this area should remain unchanged because the accumulation of the strain is minor according to the equivalent von Mises strain. In practice, however, there is a tendency towards increasing homogeneity across the disk based on strain gradient plasticity modelling [47]. Figure 4 shows that prominent morphological changes occurred at the half-radius and near the edge of the disks after HPT processing and the phases, particularly the FCC phases, underwent shear deformation so that they were elongated and bent along the direction of rotation as a result of the circumferential torsional straining. It is readily apparent that the shearing of phases and their alignment with the torsional flow paths become more pronounced with the increases in both the distance from the disk center and the number of turns. This observation is consistent with the expectation that the shear strain imposed by HPT increases with increasing distance from the disk center.

When the torsional straining is continued, the evidence for the elongation and the bending of the FCC phase associated with the torsional flow becomes less clear and is essentially lost, resulting in a reasonably homogeneous distribution of phases. Thus, distinct B2/BCC and FCC phases are no longer clearly resolvable by SEM near the edge of the disk after 1/2 turns or both at the half-radius or near the edge of the disk after 1 turn.

It is concluded that the experimental evidence in Fig. 4 demonstrates that the elongation of the FCC phase and the alignment with the torsional flow lines is mainly limited to regions

around the outer peripheries of the HPT-processed disks and this region extends towards the center with increasing numbers of turns. To further investigate the composition of the phases in the alloys after HPT processing, SEM-EDS was employed to analyze for possible chemical inhomogeneities. Fig. 5(a) shows a typical SEM-BSE image near the edge of the disk after HPT processing through 1 turn and the corresponding elemental mapping results are given in Fig. 5(b-e). It is apparent that all elements are randomly distributed without the presence of any macro-segregation or second phases and this confirms the diffusive nature of the phase transition from B2 and/or the BCC phase to the FCC phase during HPT processing.

### *3.3 Hardness along the disk radius after HPT processing*

Since the hardness distributions should exhibit reasonable radial symmetry, the hardness values plotted for randomly selected diameters should be equally applicable for any diameter across each disk. The microhardness values were recorded over three randomly selected diameters of each disk and the average values of hardness were then calculated for each position with separations of 0.5 mm. For simplicity, the results in Fig. 6 represent datum points recorded for single radii between 0 (central position) and 4 mm (near the outer edge of the disk) where an equivalence is assumed between the measurements recorded at the same distances from the center on either side of the disk. Thus, the recorded hardness values are based on a total of six separate hardness measurements except for the central position at 0 mm where there are three hardness measurements.

Fig. 6(a) shows the average values of the Vickers microhardness,  $H_v$ , plotted along the disk radius after HPT processing through varying number of turns, with the lower dotted line at  $H_v \approx 366$  corresponding to the measured hardness in the as-cast condition. The hardness

values increase with increasing distance from the central position and with increasing numbers of HPT turns. In practice, these values of Hv follow a unified trend when plotted, as suggested elsewhere [48], as a function of the equivalent strain in Fig. 6(b) which suggests an ultimate stabilization at a hardness value of  $H_v \approx 540$ . The overall trends for these hardness values are similar to earlier reports for numerous pure metals, alloys and high-entropy materials [49-51] and they follow the general trend predicted in a review of hardness evolution in HPT where this type of hardness is designated as occurring without recovery [52].

### *3.4 Tensile properties after HPT processing*

Representative plots of engineering stress versus engineering strain are shown in Fig. 7(a) using an initial strain rate of  $5 \times 10^{-4} \text{ s}^{-1}$  for the as-cast alloy and the HPT-processed alloys. The ultimate tensile strength (UTS) and yield strength (YS at the 0.2% offset) are summarized in Fig. 7(b) and plotted against the number of HPT turns. Compared to the as-cast counterpart, the HPT-processed alloys exhibit significantly higher values for the YS and UTS but significantly lower total elongations. Thus, the HPT-processed alloys exhibited elongations of typically  $\sim 5\%$  whereas the elongation for the as-cast alloy was  $\sim 38\%$ . The increase in strength but decrease in elongation after HPT processing is consistent with results for many other materials [53-55]. The larger ratio of YS over UTS by comparison with the as-cast alloy indicates a reduction in work hardening capability in the HPT-processed alloys and this is consistent with the mechanical behavior of metals after SPD processing and testing in tension [56, 57].

Fig. 7(c) and (d) show the true stress-true strain curves and the work hardening rate for the as-cast and HPT-processed alloys, where the work hardening rate,  $\theta = d\sigma/d\varepsilon$ , was derived from

the corresponding true stress-true strain curves and plotted as a function of true strain. The work hardening rate of the as-cast alloy shows a rapid initial decrease corresponding to the conventional elastic to plastic transition and thereafter a gradual and monotonical decrease with increasing true strain followed by a more rapid decrease in the later stage of deformation due to the advent of necking. The continuously decreasing work hardening rates of the as-cast alloy correlate with deformation by dislocation slip. It is apparent that all of the HPT-processed alloys show only an abrupt decrease in the work hardening rate up to the point of failure. The differences in the work hardening rates of the HPT-processed alloys is attributed to the varying dislocation densities introduced during HPT deformation.

### *3.5 Fracture characteristics in tensile testing*

In view of the transition of the elongations of the samples, it is anticipated that the fracture mode of the alloys may change in the tensile testing and this was investigated by conducting fractographic observations on the tensile fracture surfaces for both the as-cast alloy and the HPT-processed alloys. As shown in Fig. 8(a), the fracture morphology of the as-cast alloy mainly features large trench-like dimples. Generally, the deformation mechanisms of the FCC and BCC (B2) phases are different with the FCC phase deforming by dislocation planar slip to act as a soft phase but the BCC (B2) phase acting as a harder phase. During tensile deformation, the harder B2 phase is barely deformed whereas the softer FCC phase becomes stretched and gradually becomes thinner. The existence of tearing testifies to the significant necking in the soft FCC phase due to its good ductility [58]. With further deformation, the soft FCC phase becomes sufficiently hardened and the initially harder B2 phase starts to undergo more deformation. The alternating deformation of the FCC phase and the B2 and BCC phases leads

to a wavy strain distribution and provides a combination of high strength and high ductility in the as-cast alloy.

The fracture morphology of the alloy after HPT processing through 1/4 turn in Fig. 8(b) also shows trench-like dimples but they are shallower compared to those in the as-cast alloy. With increasing HPT straining, the trench-like dimples in the tensile fracture surfaces become smaller and gradually change to a globular appearance. Cleavage facets and fine ridges are also observed in the fracture surfaces of the alloys after HPT processing through 1/2 and 1 turn in Figs 8(c) and (d). The combination of cleavage facets, fine ridges and shallow dimples demonstrates that the fracture mode of the AlCrFe<sub>2</sub>Ni<sub>2</sub> HEA alloy changes from ductile fracture in the as-cast condition to a mixed character of ductile and quasi-cleavage fracture after HPT processing.

#### **4. Discussion**

It is well known that pressure or high strain-induced transformations may be activated by SPD processing but nevertheless there are very few reports of a deformation-induced phase transition in multi-phase HEAs. The present results provide a clear demonstration that the processing of the AlCrFe<sub>2</sub>Ni<sub>2</sub> alloy by HPT at room temperature produces a phase transition from the B2 and/or BCC phases to the FCC phase as demonstrated by microstructural evolutions and the variations in the intensities of the XRD peaks. In addition, the homogeneous distribution of elemental constituents after HPT processing, as shown in Fig. 5, confirm the diffusional transition nature. In metallic materials, the substitutional solutes usually have very low bulk diffusivity especially in high-entropy alloys due to the sluggish diffusion

of the constituents. In this study, the HPT processing was performed at room temperature and the calculations show that the temperature of the sample will remain only slightly above ambient since the massive HPT anvils act as effective heat sinks [44,59,60]. The duration through which the HPT-processed samples experienced an elevated temperature was up to a maximum of 60 s and the atomic mobilities of the constituents are then too low to produce significant interdiffusion. Therefore, it is concluded that the ability of HPT to transform the B2 and/or BCC phase into the FCC phase is due to the severe shear deformation and the short time required to attain a high level of strain.

The deformation mechanism occurring in dual or multiphase materials during HPT processing depends strongly on the strain path and the characteristics of the initial microstructure including the phase volume fractions and the initial size and shape of the components [61, 62]. Considering co-deformation and the subsequent deformation-induced mechanical mixing, the mechanical properties are important including the yield strength and the ultimate tensile strength as well as the work hardening of the individual phases [63,64]. In the AlCrFe<sub>2</sub>Ni<sub>2</sub> alloy, the Fe and the Cr-rich FCC solid solution phase have good ductility but low strength whereas the Al and Ni-rich B2 and BCC solid solutions exhibit high strength but poor ductility. During HPT processing, the FCC solid solution undergoes large plastic straining and exhibits an elongation in the shearing direction while the B2 and/or BCC phases are unable to deform to the same extent due to their poor ductility. The primary deformation of the FCC solid solution phase produces many dislocations which are accumulated at the FCC/B2 phase boundaries and, as a result, more dislocations are activated in the B2 and/or BCC phase. At this stage, the stress in the phase boundaries is released and plastic deformation is initiated in the

B2 and/or BCC phases which are sectioned by the gliding dislocations. With increasing strain, the FCC phase and the B2 and/or BCC phases are repeatedly deformed and fractured and so that their sizes are continuously refined.

From this perspective, the mechanism controlling the transformation from the B2 and/or BCC phases to the FCC phase driven by HPT processing is similar to the transformation driven by mechanical alloying during which the transition takes place by enhanced diffusion which is mainly affected by the diffusion distance and diffusive activation energy [65, 66]. The high shear strain in HPT induces a high density of defects, such as dislocations and vacancies, and this reduces the apparent activation energy of diffusion that provides the chemical driving force for elemental diffusion. During the mass transfer in HPT, an external action forces the atoms to overcome an energy barrier which is similar to that for bulk diffusion. The high diffusion coefficient during HPT processing is due primarily to the extremely high concentration of non-equilibrium vacancies [67, 68]. The severe deformation of the FCC phase and the B2 and/or BCC phase yields large areas of active fresh surfaces which are continuously brought together with interdiffusion occurring between the particles. The reduced length scale of both the FCC phase and the B2 and/or BCC phases increases the kinetics of the transition from the B2 and/or BCC phases to the FCC phase. Therefore, it is reasonable to assume that the introduction of defects and the enhanced diffusion are responsible for the observed phase transition under HPT deformation [69,70]. This phase transition occurs through intensive mass transfer whereby Fe and Cr atoms diffuse from the FCC phase to the B2 and/or BCC phase while the Ni and Al atoms diffuse from the B2 and/or BCC phase to the FCC phase. However, additional detailed experiments and measurements are needed to obtain a thorough understanding of the

mechanisms responsible for the phase transformation in multi-phase HEA under HPT.

The level of HPT deformation demonstrates an important impact on the mechanical properties of the AlCrFe<sub>2</sub>Ni<sub>2</sub> HEA. The HPT deformation induces increases in hardness and strength of the AlCrFe<sub>2</sub>Ni<sub>2</sub> alloy and this is due to multiple factors including the defect factor (especially the introduction of dislocations), the phase factor (crystal structure and solid solution strengthening) and the morphological factor due to grain refinement [71, 72]. Under HPT deformation, the high density dislocations continue to grow and accumulate in the FCC phase and the intensified interactions between dislocations result in dislocation entanglements or dislocation jogs which hinder any further movement of dislocations. This leads to work hardening even though the number of rotations was limited to 1. The deformation induced transition from B2 and/or the BCC phase to the FCC phase results in solid solution strengthening due to the incorporation of Al atoms with a larger atomic radius within the FCC crystal lattice. The formation of subgrains, as in the grain refinement, leads to grain boundary strengthening.

The decreased tensile ductility of the HPT-processed alloys results from the microscopic crack initiation caused by large stress concentrations due to the high density of dislocations and the reduced grain size, and this produces an early plastic instability caused by the lack of strain-hardening capability. Consistent with the observation of the smaller and shallower dimples in the fractural surfaces, it may be concluded that a ductile and quasi-cleavage mixed fracture mechanism governed the tensile response of the HPT-processed alloys. The dimples represent the interfacial separation of the matrix from other structural features, including tangles of dislocations and grain boundaries, due to their strain capacity differences when the strain

restriction imposed to the matrix allows an interfacial detachment combined with a simultaneous growth and coalescence of microvoids. Thus, more tangles of dislocations and fine grains lead to increased microvoid nucleation and this will shorten the critical strain to fracture since coalescence can occur more quickly.

Generally, chemical homogenization is achieved in materials by elevating the temperature and then quenching to room temperature. As indicated by the XRD and EDS analyses documented in this report, the high strain imposed by HPT introduces atomic mixing at room temperature in the AlCrFe<sub>2</sub>Ni<sub>2</sub> alloy and causes a microstructure which is preserved kinetically although thermodynamically unfavorable. It seems probable that at this point the steady-state concentration of second components, such as Al and Ni in the FCC solid solution, may be the same after HPT processing as in the alloy after subjecting to a long anneal at an elevated temperature. This suggests the potential for beneficially employing a post-HPT heat treatment, as used in some other research programs [73, 74], in order to achieve better combinations of strength and ductility. Further experiments are necessary to more fully explore this possibility.

## **5. Summary and conclusions**

1. The solidification of the AlCrFe<sub>2</sub>Ni<sub>2</sub> HEA follows the sequence of pre-eutectic FCC phase, FCC+B2 binary eutectics and FCC+B2+BCC ternary eutectics. The BCC and B2 phases are enriched in Ni and Al while the FCC phase is enriched in Fe and Cr.
2. Processing by HPT up to 1 turn produces a phase transition from the B2 and/or BCC phases to the FCC phase. A reasonably homogeneous chemical composition is obtained when applying a sufficient level of torsional strain and this supports the diffusional nature of the transformation.

3. The HPT processing leads to an increase in hardness and strength but a corresponding decrease in elongation in tensile testing at room temperature. The fracture behaviour changes from ductile in the initial as-cast condition to mixed characteristics of ductile and quasi-cleavage fracture after HPT processing.
4. By analogy with mechanical alloying, the effect of HPT processing on the phase transition is a consequence of the severe shear-induced mechanical mixing which takes place by enhanced diffusion due to the introduction of defects and the reduction of length scale of various phases during the HPT.

### **Acknowledgements**

This work was funded by the In-house funding from the Key Lab of EPM of NEU (grant number: NEU-EPM-002). The work of two of the authors was supported by the European Research Council under ERC Grant Agreement No. 267464-SPDMETALS (YH and TGL).

### **Data Availability**

The raw/processed data required to reproduce these findings cannot be shared at this time as the data also forms part of an ongoing study.

## References

- [1] J. W. Yeh, S. K. Chen, S. J. Lin, J. Y. Gan, T. S. Chin, T. T. Shun, C. H. Tsau, S. Y. Chang, Nanostructured high-entropy alloys with multiple principal elements: novel alloy design concepts and outcomes, *Adv. Eng. Mater.* 6 (2004) 299-303.
- [2] Y. Zhang, T. T. Zuo, Z. Tang, M. C. Gao, K. A. Dahmen, P. K. Liaw, Z. P. Lu, Microstructures and properties of high-entropy alloys, *Prog. Mater. Sci.* 61 (2004) 1-93.
- [3] K. M. Youssef, A. J. Zaddach, C. Niu, D. L. Irving, C. C. Koch, A novel low-density, high-hardness, high-entropy alloy with close-packed single-phase nanocrystalline structures, *Mater. Res. Lett.* 2 (2014) 95-99.
- [4] Y. F. Ye, Q. Wang, J. Lu, C. T. Liu, Y. Yang, High-entropy alloy: challenges and prospects, *Mater. Today* 19 (2015) 349-362.
- [5] D. B. Miracle, O. N. Senkov, A critical review of high entropy alloys and related concepts, *Acta Mater.* 122 (2017) 448-511.
- [6] Z. P. Lu, H. Wang, M. W. Chen, I. Baker, J. W. Yeh, C. T. Liu, T. G. Nieh, An assessment on the future development of high-entropy alloys: summary from a recent workshop, *Intermetallics* 66 (2015) 67-76.
- [7] J. Chen, X. Y. Zhou, W. L. Wang, B. Liu, Y. K. Lv, W. Yang, D. P. Xu, Y. Liu, A review on fundamental of high entropy alloys with promising high-temperature properties, *J. Alloys Compd.* 760 (2018) 15-30.
- [8] B. Cantor, I. T. H. Chang, P. Knight, A. J. B. Vincent, Microstructural development in equiatomic multicomponent alloys, *Mater. Sci. Eng. A* 357 (2004) 213-218.
- [9] O. N. Senkov, J. D. Miller, D. B. Miracle, C. Woodward, Accelerated exploration of multi-

principal element alloys with solid solution phases, *Nat. Commun.* 7529 (2015) 1-7.

[10] S. Gorsse, D. B. Miracle, O. N. Senkov, Mapping the world of complex concentrated alloys, *Acta Mater.* 135 (2017) 177-187.

[11] J. P. Couzynie, G. Dirras, Body-centered cubic high-entropy alloys: From processing to underlying deformation mechanisms, *Mater. Character.* 147 (2019) 533-544.

[12] H. L. Huang, Y. Wu, J. Y. Yeh, H. Wang, X. J. Liu, K. An, W. Wu, Z. P. Lu, Phase-Transformation ductilization of brittle high-entropy alloys via metastability engineering, *Adv. Mater.* 170168 (2017) 1-7.

[13] Y. P. Lu, Y. Dong, S. Guo, L. Jiang, H. J. Kang, T. M. Wang, B. Wen, Z. J. Wang, J. C. Jie, Z. Q. Cao, H. H. Ruan, T. J. Li, A promising new class of high-temperature alloys: eutectic high-entropy alloys, *Sci. Rep.* 4 (2014) 6200.

[14] F. He, Z. Wang, P. Cheng, Q. Wang, J. Li, Y. Dang, J. Wang, C. T. Liu, Designing eutectic high entropy alloys of  $\text{CoCrFeNiNb}_x$ , *J. Alloys Compd.* 656 (2016) 284-289.

[15] Q. F. Wu, Z. J. Wang, T. Zeng, D. Chen, Z. S. Yang, J. J. Li, J. J. Kai, J. C. Wang, A casting eutectic high entropy alloy with superior strength-ductility combination, *Mater. Lett.* 253 (2019) 268-271.

[16] X. Jin, Y. X. Liang, L. Zhang, J. Bi, Y. Zhou, B. S. Li, Back stress strengthening dual-phase  $\text{AlCoCr}_2\text{FeNi}_2$  high entropy alloy with outstanding tensile properties, *Mater. Sci. Eng. A* 745 (2019) 137-143.

[17] Y. P. Lu, X. Z. Gao, J. Jiang, Z. N. Chen, T. M. Wang, J. C. Jie, H. J. Kang, Y. B. Zhang, S. Guo, H. H. Ruan, Y. H. Zhao, Z. Q. Cao, T. J. Li, Directly cast bulk eutectic and near eutectic high entropy alloys with balanced strength and ductility in a wide temperature range, *Acta*

Mater. 124 (2017) 143-150.

[18] S. G. Ma, J. W. Qiao, Z. H. Wang, H. J. Yang, Y. Zhang, Microstructural features and tensile behaviors of the Al<sub>0.5</sub>CrCuFeNi<sub>2</sub> high-entropy alloys by cold rolling and subsequent annealing, Mater. Des. 88 (2015) 1057-1062.

[19] A. P. Zhilyaev, T. G. Langdon, Using high-pressure torsion for metal processing: Fundamentals and applications, Prog. Mater. Sci. 53 (2008) 893-979.

[20] C. Gammer, C. Mangler, H. P. Karnthaler, C. Rentenberger, Anomalous re-ordering of Fe<sub>3</sub>Al disordered by high pressure torsion deformation, Scripta Mater. 156 (2018) 90-94.

[21] B. B. Straumal, A. R. Kilmametov, A. Korneva, A. A. Mazilkin, P. B. Straumal, P. Zieba, B. Baretzky, Phase transitions in Cu-based alloys under high pressure torsion, J. Alloys Compd. 707 (2017) 20-26.

[22] N. Ibrahim, M. Peterlechner, F. Emeis, M. Wegner, S. V. Divinski, G. Wilde, Mechanical alloying via high-pressure torsion of the immiscible Cu<sub>50</sub>Ti<sub>50</sub> system, Mater. Sci. Eng. A 685 (2017) 19-30.

[23] R. Kulagin, Y. Beygelzimer, Y. Ivanisenko, A. Mazilkin, B. Straumal, H. Hahn, Instabilities of interfaces between dissimilar metals induced by high pressure torsion, Mater. Lett. 222 (2018) 172-175.

[24] Y. Sun, M. Aindow, R. J. Hebert, T. G. Langdon, E. J. Lavernia, High-pressure torsion-induced phase transformations and grain refinement in Al/Ti composites, J. Mater. Sci. 52 (2017) 12170-12184.

[25] N. X. Zhang, M. Kawasaki, Y. Huang, T. G. Langdon, Microstructural evolution in two-phase alloys processed by high-pressure torsion, J. Mater. Sci. 48 (2013) 4582-4591.

- [26] B. Straumal, A. Korneva, P. Zieba, Phase transitions in metallic alloys driven by the high pressure torsion, *Arch. Civ. Mech. Eng.* 14 (2014) 242-249.
- [27] Y. Ivanisenko, W. Lojkowski, R. Z. Valiev, H. J. Fecht, The mechanism of formation of nanostructure and dissolution of cementite in a pearlite steel during high pressure torsion, *Acta Mater.* 51 (2003) 5555-5570.
- [28] P. Henits, Á. Révész, A. P. Zhiyaev, Z. Kovács, Severe plastic deformation induced nanocrystallization of melt-spun Al<sub>85</sub>Y<sub>8</sub>Ni<sub>5</sub>Co<sub>2</sub> amorphous alloy, *J. Alloys Compd.* 461 (2008) 195-199.
- [29] A. V. Sergueeva, C. Song, R. Z. Valiev, A. K. Mukherjee, Structure and properties of amorphous and nanocrystalline NiTi prepared by severe plastic deformation and annealing, *Mater. Sci. Eng. A* 339 (2003) 159-165.
- [30] Y. F. Sun, H. Fuji, T. Nakamura, N. Tsuji, D. Todaka, M. Umemoto, Critical strain for mechanical alloying of Cu-Ag, Cu-Ni and Cu-Zr by high-pressure torsion, *Scripta Mater.* 65 (2011) 489-492.
- [31] Y. Cao, S. Ni, X. Z. Liao, M. Song, Y. T. Zhu, Structural evolutions of metallic materials processed by severe plastic deformation, *Mater. Sci. Eng. R* 133 (2018) 1-59.
- [32] Y. B. Wang, X. Z. Liao, Y. H. Zhao, J. C. Cooley, Z. Horita, Y. T. Zhu, Elemental separation in nanocrystalline Cu-Al alloys, *Appl. Phys. Lett.* 102 (2013) 231912
- [33] A. A. Mazilkin, B. B. Straumal, E. Rabkin, B. Baretzky, S. Enders, S. G. Protasova, O. A. Kogtenkova, R. Z. Valiev, Softening of nanostructured Al-Zn and Al-Mg alloys after severe plastic deformation, *Acta Mater.* 54 (2006) 3933-3939

- [34] B. Schuh, F. Mendez-Martin, B. Volker, E. P. George, H. Clemens, R. Pippan, A. Hohenwarter, Mechanical properties, microstructure and thermal stability of a nanocrystalline CoCrFeMnNi high-entropy alloy after sever plastic deformation, *Acta Mater.* 96 (2015) 258-268.
- [35] H. Shahmir, J. Y. He, Z. P. Lu, M. Kawasaki, T. G. Langdon, Effect of annealing on mechanical properties of a nanocrystalline CoCrFeMnNi high-entropy alloy processed by high-pressure torsion, *Mater. Sci. Eng. A* 676 (2016) 294-303.
- [36] A. Kilmametov, R. Kulagin, A. Mazikin, S. Seils, T. Boll, M. Heilmaier, H. Hahn, High-pressure torsion driven mechanical alloying of CoCrFeMnNi high entropy alloy, *Scripta Mater.* 158 (2019) 29-33.
- [37] A. Heczal, M. Kawasaki, J. L. Lábár, J. I. Jang, T. G. Langdon, J. Gubicza, Defect structure and hardness in nanocrystalline CoCrFeMnNi high-entropy alloy processed by high-pressure torsion, *J. Alloys Compd.* 71 (2017) 143-154.
- [38] W. Q. Wu, M. Song, S. Ni, J. S. Wang, Y. Liu, B. Liu, X. Z. Liao, Dual mechanisms of grain refinement in a FeCoCrNi high-entropy alloy processed by high-pressure torsion, *Sci. Rep.* 46720 (2017) 1-13.
- [39] P. F. Yu, H. Chen, L. J. Zhang, H. Zhang, Q. Jing, M. Z. Ma, P. K. Liaw, G. Li, R. P. Liu, Effects of high pressure torsion on microstructures and properties of an Al<sub>0.1</sub>CoCrFeNi high-entropy alloy, *Mater. Sci. Eng. A* 655 (2016) 283-291.
- [40] R. X. Zheng, J. Chen, W. L. Xiao, C. L. Ma, Microstructure and tensile properties of nanocrystalline (FeNiCoCu)<sub>1-x</sub>Ti<sub>x</sub>Al<sub>x</sub> high entropy alloys processed by high pressure torsion, *Intermetallics* 74 (2016) 38-45.

- [41] Q. H. Tang, Y. Huang, Y. Y. Huang, X. Z. Liao, T. G. Langdon, P. Q. Dai, Hardening of an  $\text{Al}_{0.3}\text{CoCrFeNi}$  high entropy alloy via high-pressure torsion and thermal annealing, *Mater. Lett.* 151 (2015) 126-129.
- [42] W. Q. Wu, S. Ni, Y. Liu, B. Liu, M. Song, Amorphization at twin-twin intersected region in  $\text{FeCoCrNi}$  high-entropy alloy subjected to high-pressure torsion, *Mater. Character.* 127 (2017) 111-115.
- [43] Q. Tang, Y. Huang, H. Cheng, X. Liao, T.G. Langdon, P. Dai, The effect of grain size on annealing-induced phase transformation in an  $\text{Al}_{0.3}\text{CoCrFeNi}$  high entropy alloy, *Mater. Design* 105 (2016) 381-385.
- [44] R. B. Figueiredo, P. H. R. Pereira, M. T. P. Aguilar, P. R. Cetlin, T. G. Langdon, Using finite element modelling to examine the flow processes in quasi-constrained high-pressure torsion, *Acta Mater.* 60 (2012) 3190-3198.
- [45] L. J. Santodonato, Y. Zhang, M. Feygenson, C. M. Parish, M. C. Gao, R. J. K. Weber, J. C. Neufeind, Z. Tang, P. K. Liaw, Deviation from high-entropy configurations in the atomic distributions of a multi-principal-element alloy, *Nat. Commun.* 6 (2015) 5964.
- [46] Y. Dong, X. Gao, Y. Lu, T. Wang, T. J. Li, A multi-component  $\text{AlCrFe}_2\text{Ni}_2$  alloy with excellent mechanical properties, *Mater. Lett.* 169 (2016) 62-64.
- [47] Y. Estrin, A. Molotnikov, C. H. J. Davies, R. Lapovok, Strain gradient plasticity modelling of high-pressure torsion, *J. Mech. Phys. Solids* 56 (2008) 1186-1202.
- [48] A. Vorhauer, R. Pippan, On the homogeneity of deformation by high pressure torsion, *Scripta Mater.* 51 (2004) 921-925.
- [49] M. Kawasaki, S. N. Alhajeri, C. Xu, T. G. Langdon, The development of hardness

homogeneity in pure aluminum and aluminum alloy disks processed by high-pressure torsion, *Mater. Sci. Eng. A* 529 (2011) 345-351.

[50] H. Shahmir, J. He, Z. Lu, M. Kawasaki, T. G. Langdon, Effect of annealing on mechanical properties of an nanocrystalline CoCrFeNiMn high-entropy alloy processed by high-pressure torsion, *Mater. Sci. Eng. A* 676 (2016) 294-303.

[51] W. T. Sun, X. G. Qiao, M. Y. Zheng, N. Hu, N. Gao, M. J. Starink, Evolution of long-period stacking ordered structure and hardness of Mg-8.2Gd-3.8Y-1.0Zn-0.4Zr alloy during processing by high pressure torsion, *Mater. Sci. Eng. A* 738 (2018) 238-252.

[52] M. Kawasaki, Different models of hardness evolution in ultrafine-grained materials processed by high-pressure torsion, *J. Mater. Sci.* 49 (2014) 18-34.

[53] N. Krasilnikov, W. Lojkowski, Z. Pakiel, R. Valiev, Tensile strength and ductility of ultrafine-grained nickel processed by severe plastic deformation, *Mater. Sci. Eng. A* 397 (2005) 330-337.

[54] N. Lugo, N. Llorca, J. M. Cabrera, Z. Horita, Microstructures and mechanical properties of pure copper deformed severely by equal-channel angular pressing and high pressure torsion, *Mater. Sci. Eng. A* 477 (2008) 366-371.

[55] R. Z. Valiev, N. A. Enikeev, M. Y. Murashkin, V. U. Kazykhanov, X. Sauvage, On the origin of the extremely high strength of ultrafine-grained Al alloys produced by severe plastic deformation, *Scr. Mater.* 63 (2010) 949-951.

[56] I. Sabirov, M. Y. Murashkin, R. Z. Valeiv, Nanostructured aluminium alloys produced by severe plastic deformation: New horizons in development, *Mater. Sci. Eng. A* 560 (2013) 1-24.

[57] I. A. Ovid'ko, R. Z. Valiev, Y. T. Zhu, Review on superior strength and enhanced ductility

of metallic nanomaterials, *Prog. Mater. Sci.* 94 (2018) 462-540.

[58] L. Wang, C. L. Yao, J. Shen, Y. P. Zhang, T. Wang, Y. H. Ge, L. H. Gao, G. J. Zhang, Microstructures and room temperature tensile properties of as-cast and directionally solidified AlCoCrFeNi<sub>2.1</sub> eutectic high-entropy alloy, *Intermetallics* 118 (2020) 106681.

[59] P. H. R. Pereira, R. B. Figueiredo, Y. Huang, P. R. Cetlin, T. G. Langdon, Modeling the temperature rise in high-pressure torsion, *Mater. Sci. Eng. A* 593 (2014) 185-188.

[60] K. Edalati, Y. Hashiguchi, P. H. R. Pereira, Z. Horita, T. G. Langdon, Effect of temperature rise on microstructural evolution during high-pressure torsion, *Mater. Sci. Eng. A* 714 (2018) 167-171.

[61] Z. C. Cordero, C. A. Schuh, Phase strength effects on chemical mixing in extensively deformed alloys, *Acta Mater.* 82 (2015) 123-136

[62] K. J. Chu, W. W. Zhu, C. C. Zhao, F. Z. Ren, Forced atomic mixing of immiscible Nb-Ag alloys by severe plastic deformation, *Mater. Lett.* 207 (2017) 141-144

[63] Y. Ashkenazy, N. Q. Vo, D. Schwen, R. S. Averbach, P. Bellon, Shear induced chemical mixing in heterogeneous systems, *Acta Mater.* 60 (2012) 984-993.

[64] A. Bachmaier, H. Aboulfadl, M. Pfaff, F. Mucklich, C. Motz, Structural evolution and strain induced mixing in Cu-Co composites studied by transmission electron microscopy and atom probe tomography, *Mater. Character.* 100 (2015) 178-191.

[65] C. Suryanarayana, Mechanical alloying and milling, *Prog. Mater. Sci.* 46 (2001) 1-184.

[66] S. Romankov, Y. C. Park, I. V. Shehetinin, J. M. Yoon, Atomic-scale intermixing amorphization and microstructural development in a multicomponent system subjected to surface severe plastic deformation, *Acta Mater.* 61 (2013) 1254-1265.

- [67] T. Ungár, E. Schafler, P. Hanák, S. Bernstorff, M. Zehetbauer, Vacancy production during plastic deformation in copper determined by in situ X-ray diffraction, *Mater. Sci. Eng. A* 462 (2007) 398-401.
- [68] J. Čížek, M. Janeček, O. Srba, R. Kužel, Z. Barnovska, I. Procházka, S. Dobatkin, Evolution of defects in copper deformed by high-pressure torsion, *Acta Mater.* 59 (2011) 2322-2329.
- [69] F. Delogu, Are processing conditions similar in ball milling and high-pressure torsion? The case of the tetragonal-to-monoclinic phase transition in ZrO<sub>2</sub> powders, *Scripta Mater.* 67 (2012) 340-343
- [70] Q. Q. Shao, J. M. Guo, J. H. Chen, Z. L. Zhang, Atomic-scale investigation on the structural evolution and deformation behaviors of Cu-Cr nanocrystalline alloys processed by high-pressure torsion, *J. Alloys Compd.* 832 (2020) 154994
- [71] T. Maity, K. G. Prashanth, O. Blaci, J. T. Kim, T. Schoberl, Z. Wang, J. Eckert, Influence of severe straining and strain rate on the evolution of dislocation structures during micro-/nanoindentation in high entropy lamellar eutectics, *Int. J. Plast.* 109 (2018) 121-136
- [72] T. Marity, O. Balci, C. Gammer, E. Ivanov, J. Eckert, K. G. Prashanth, High pressure torsion induced lowering of Young's modulus in high strength TNZT alloy for bio-implant applications, *Journal of the Mechanical Behavior of Biomedical Materials* 108 (2020) 103839
- [73] S. A. Torbati-Sarraf, S. Sabbaghianrad, T. G. Langdon, Using post-deformation annealing to optimize the properties of a ZK60 magnesium alloy processed by high-pressure torsion, *Adv. Eng. Mater.* 20 (2018) 1700703.
- [74] H. Shahmir, M. Nili-Ahmadabadi, M. Mohammadi, Y. Huang, M. Andrzejczuk, M.

Lewandowska, T. G. Langdon, Effect of Cu on amorphization of a TiNi alloy during HPT and shape memory effect after post-deformation annealing, *Adv. Eng. Mater.* 22 (2020) 1900387.

## Figure Captions

**Fig. 1** (a) Solidification calculation for the as-cast AlCrFe<sub>2</sub>Ni<sub>2</sub> alloy, (b) BSE image of the as-cast alloy and (c) enlargement of region C in (b)

**Fig. 2** SEM-EDS elemental mapping of Al, Cr, Fe and Ni for the as-cast alloy: (a) SEM image and mapping for (b) Al, (c) Cr, (d) Fe and (e) Ni.

**Fig. 3** (a) XRD analysis for the as-cast sample and after HPT through 1/4, 1/2 and 1 turn, (b) enlarged images of the major peaks and (c) lattice constants of the FCC phase and the B2/BCC phase

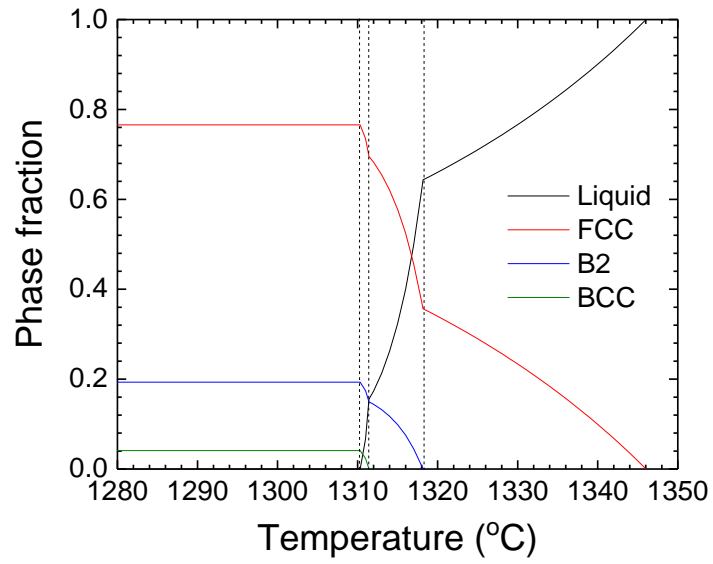
**Fig. 4** SEM-BSE images showing the microstructure at the center, half-radius and edge of the disks after HPT for 1/4, 1/2 and 1 turn

**Fig. 5** SEM-EDS elemental mapping of Al, Cr, Fe and Ni at the edge of the disk after HPT processing for 1 turn: (a) SEM image and mapping for (b) Al, (c) Cr, (d) Fe and (e) Ni.

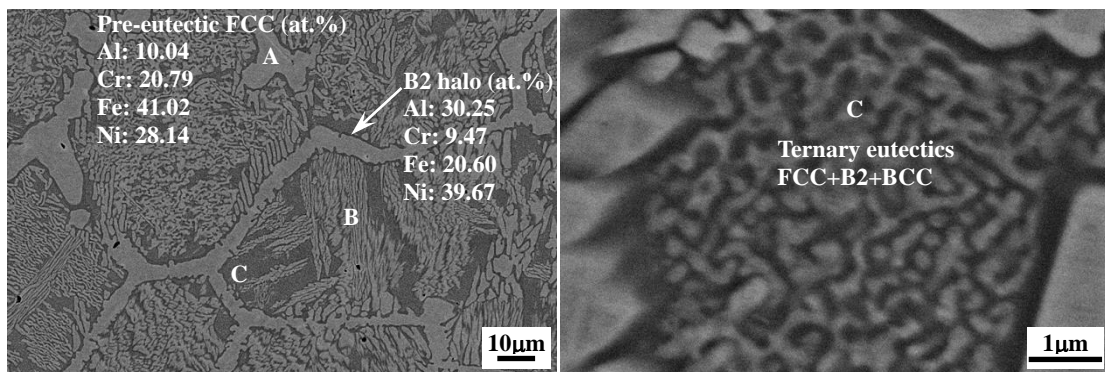
**Fig. 6** The Vickers microhardness plotted against (a) distance from the disk center and (b) equivalent strain for samples processed by HPT through 1/4, 1/2 and 1 turn.

**Fig. 7** Tensile properties of the alloys in the as-cast condition and after HPT processing through various turns: (a) Engineering stress-engineering strain curves, (b) UTS, YS and elongation derived from the engineering stress-engineering strain curves, (c) true stress-true strain curves and (d) work hardening rate plotted against true strain.

**Fig. 8** SEM images of the fracture surfaces of the samples after tensile testing (a) for the as-cast alloy and processing by HPT through (b) 1/4 turn, (c) 1/2 turn and (d) 1 turn.



(a)



(b)

(c)

**Fig. 1** (a) Solidification calculation for the as-cast AlCrFe<sub>2</sub>Ni<sub>2</sub> alloy, (b) BSE image of the as-cast alloy and (c) enlargement of region C in (b)

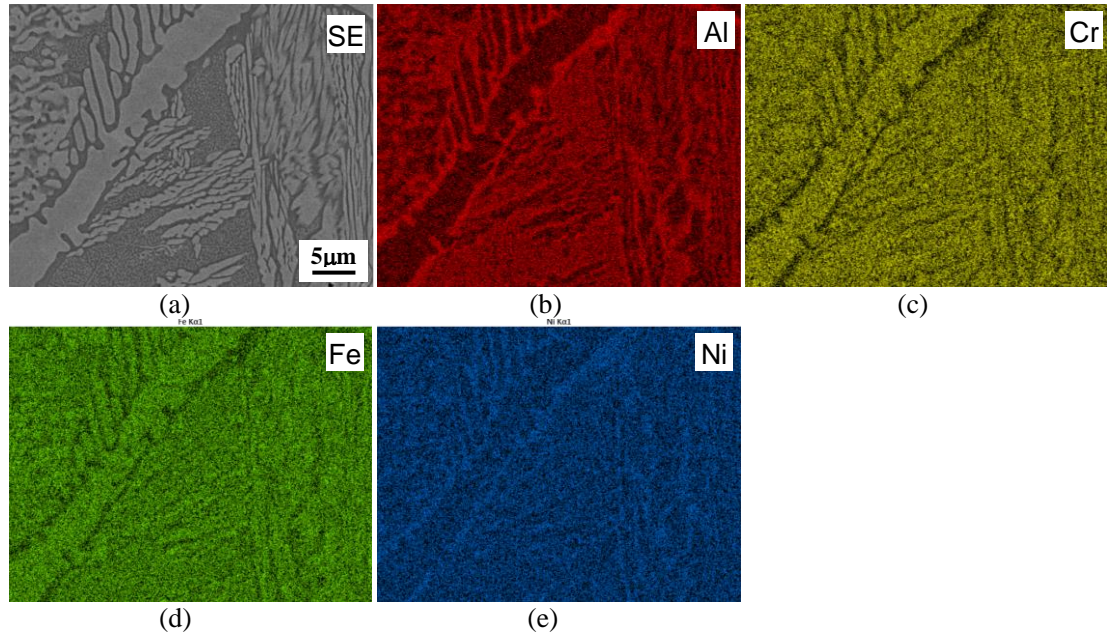


**Fig. 2** SEM-EDS elemental mapping of Al, Cr, Fe and Ni for the as-cast alloy: (a) SEM image and mapping for (b) Al, (c) Cr, (d) Fe and (e) Ni.

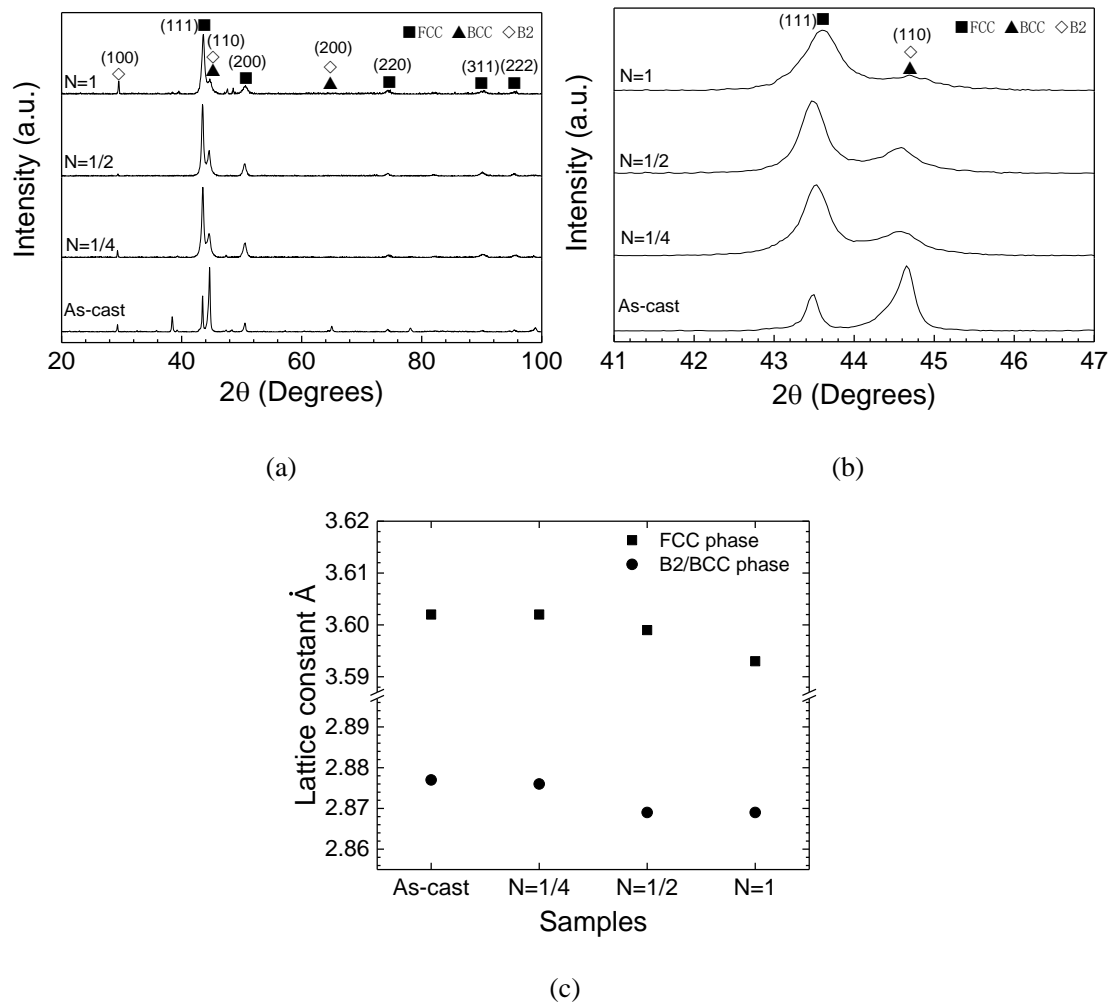


**Fig. 3** (a) XRD analysis for the as-cast sample and after HPT through 1/4, 1/2 and 1 turn, (b) enlarged images of the major peaks and (c) lattice constants of the FCC phase and the B2/BCC phase

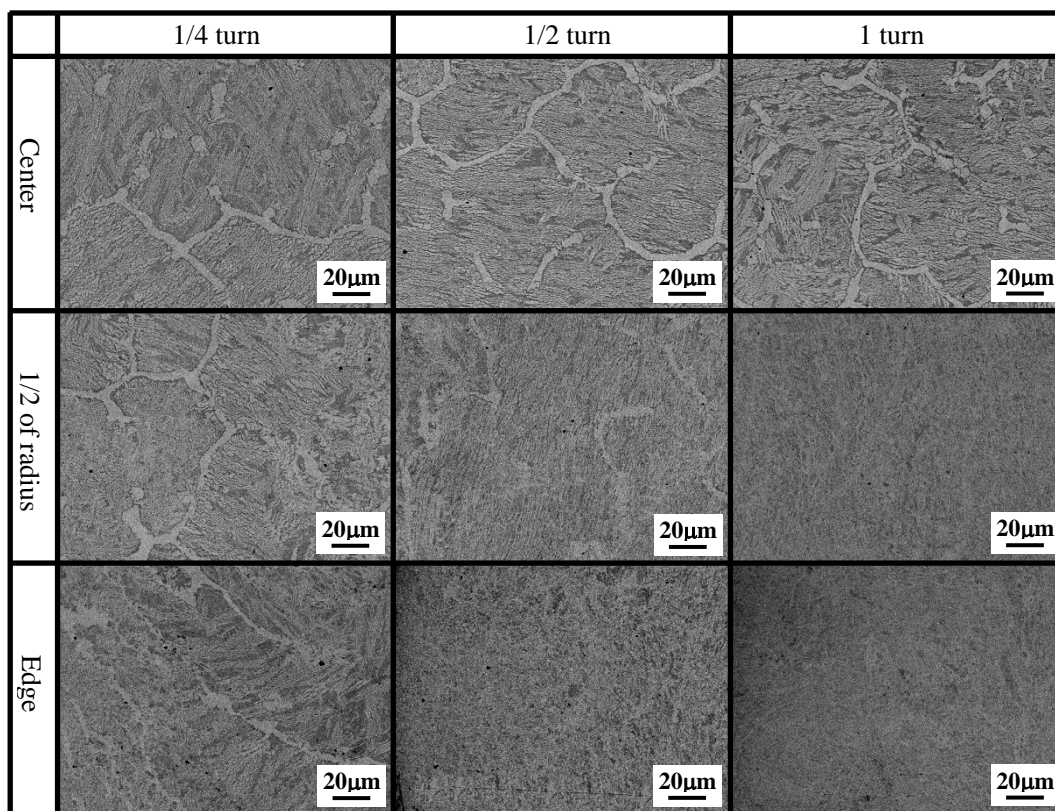


**Fig. 4** SEM-BSE images showing the microstructure at the center, half-radius and edge of the disks after HPT for 1/4, 1/2 and 1 turn

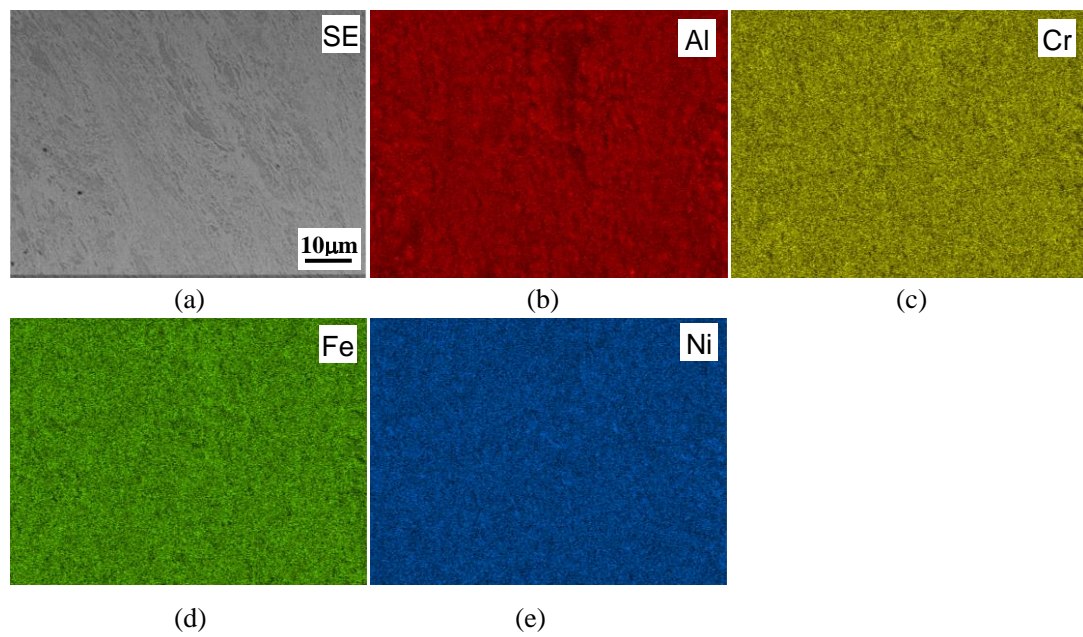


**Fig. 5** SEM-EDS elemental mapping of Al, Cr, Fe and Ni at the edge of the disk after HPT processing for 1 turn: (a) SEM image and mapping for (b) Al, (c) Cr, (d) Fe and (e) Ni

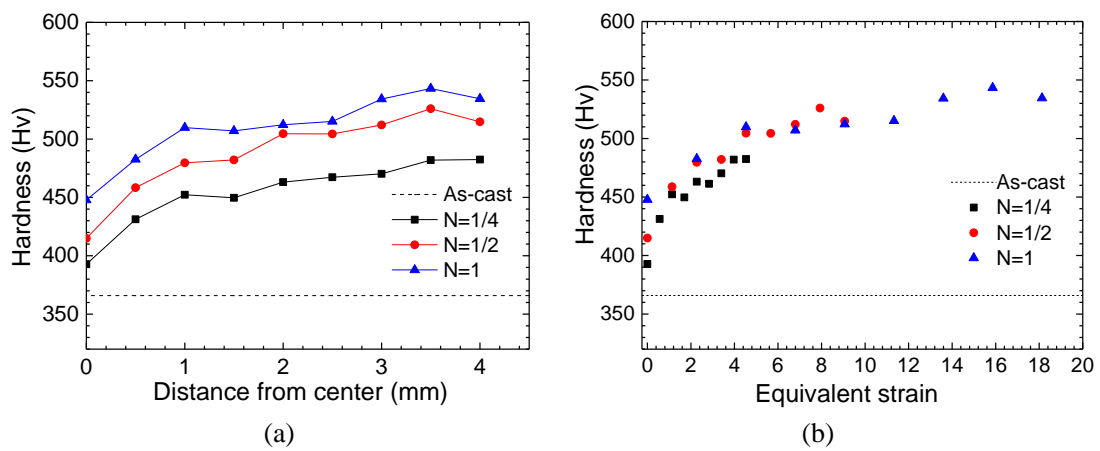


**Fig. 6** The Vickers microhardness plotted against (a) distance from the disk center and (b) equivalent strain for samples processed by HPT through 1/4, 1/2 and 1 turn

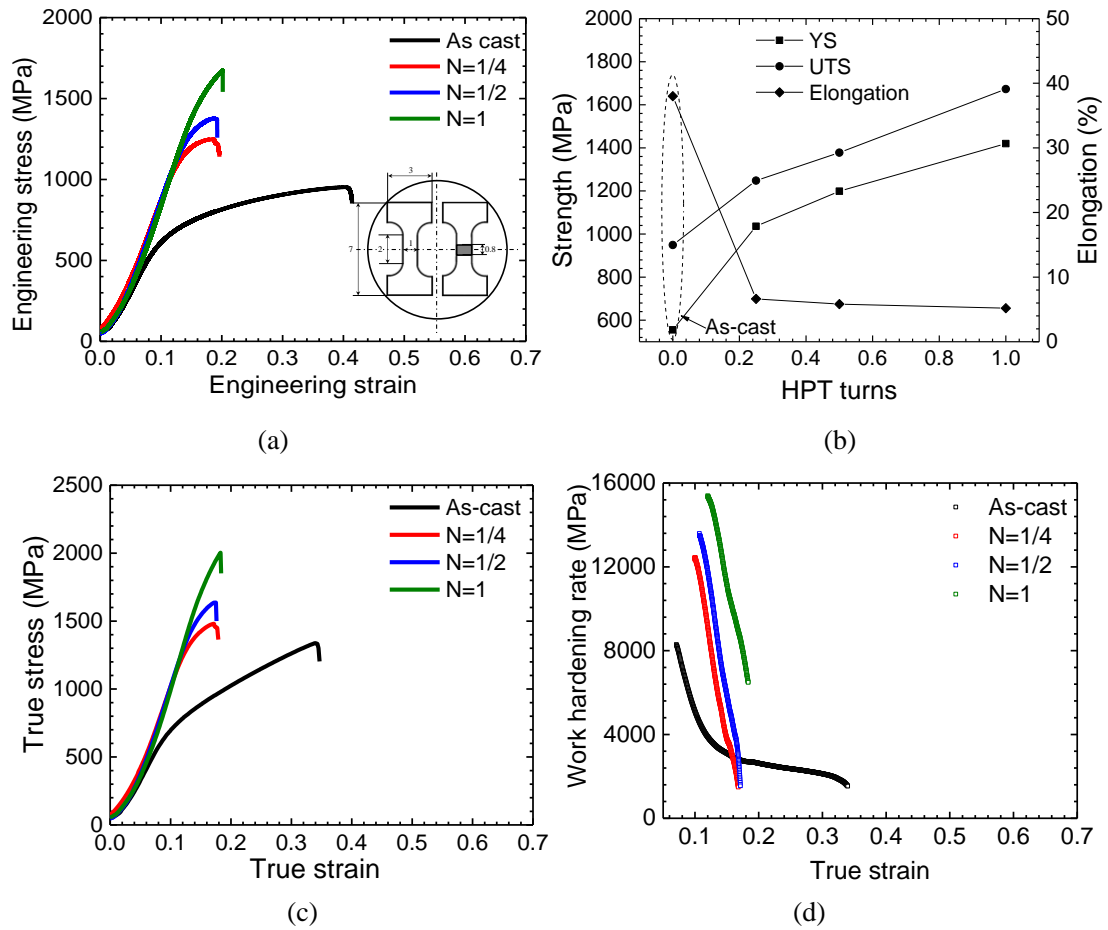


**Fig. 7** Tensile properties of the alloys in the as-cast condition and after HPT processing through various turns: (a) Engineering stress-engineering strain curves, (b) UTS, YS and elongation derived from the engineering stress-engineering strain curves, (c) true stress-true strain curves and (d) work hardening rate plotted against true strain

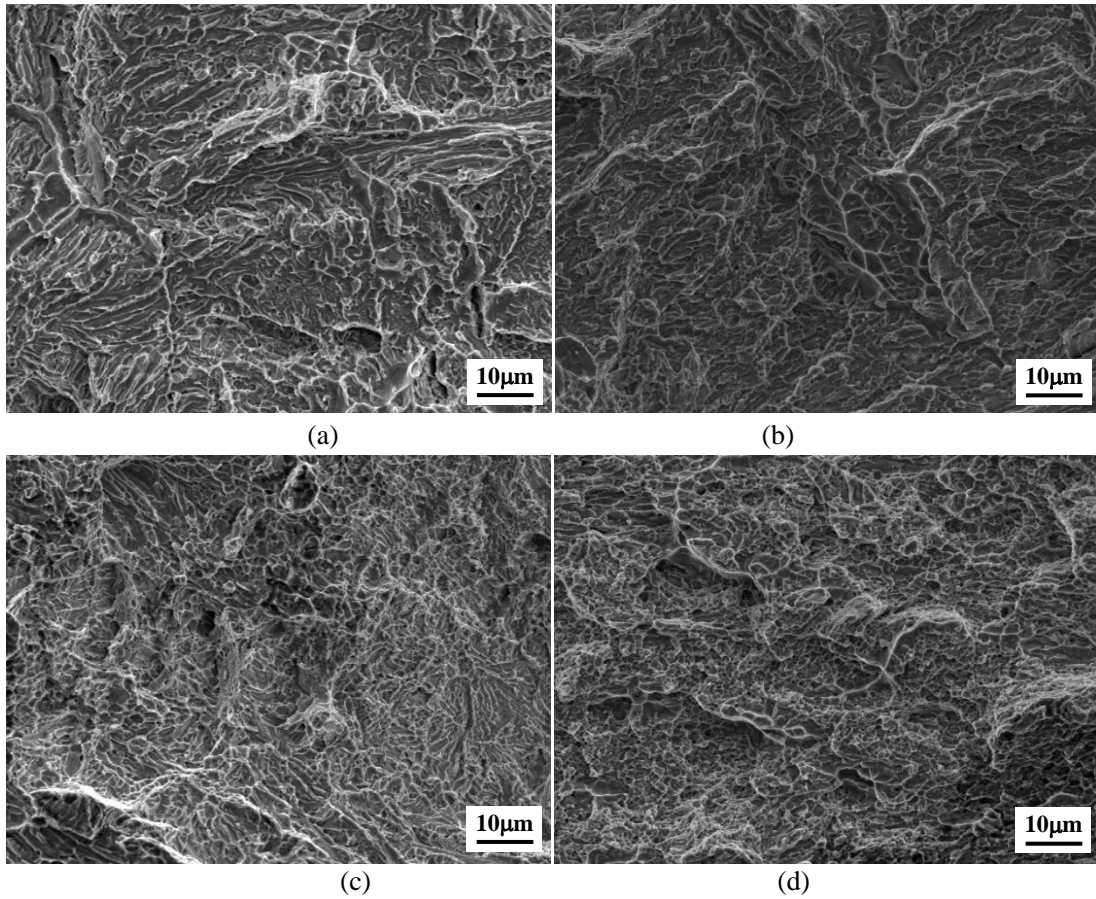


**Fig. 8** SEM images of the fracture surfaces of the samples after tensile testing (a) for the as-cast alloy and processing by HPT through (b) 1/4 turn, (c) 1/2 turn and (d) 1 turn